N94-34969

Unsteady Flow Past an Airfoil Pitched at Constant Rate

by L. Lourenco, L. Van Dommelen, C. Shih & A. Krothapalli

Department of Mechanical Engineering
FAMU/FSU College of Engineering
Tallahassee, FL 32316-2175
Florida A & M University and Florida State University

This program is sponsored by AFOSR

Abstract

The unsteady flow past a NACA 0012 airfoil that is undertaking a constant-rate pitching up motion is investigated experimentally by the PIDV technique in a water towing tank. The Reynolds number is 5000, based upon the airfoil's chord and the free-stream velocity. The airfoil is pitching impulsively from 0 to 30° with a dimensionless pitch rate $\dot{\alpha}$ of 0.131. Instantaneous velocity and associated vorticity data have been acquired over the entire flow field. The primary vortex dominates the flow behavior after it separates from the leading edge of the airfoil. Complete stall emerges after this vortex detaches from the airfoil and triggers the shedding of a counter-rotating vortex near the trailing edge. A parallel computational study using the discrete vortex, random walk approximation has also been conducted. In general, the computational results agree very well with the experiment.

1. Introduction

Due to the recent interest in developing a supermaneuverable fighter aircraft, a complete knowledge of the unsteady flow behavior over a wing is necessary in order to improve the post stall aerodynamic performance. Although much progress has been made both experimentally and numerically throughout the years,[1,2] a fundamental understanding of the problem is still lacking. The difficulty mainly arises from the fact that these flows are extremely complex and are not amenable to standard experimental and numerical techniques. For example, one of the most important feature about the flow past an unsteady airfoil is the emergency of one or several large scale vortical eddies after the flow separates from the upper surface. Later evolution of these vortical structures dominate the behavior of the flow past the airfoil's surface. They either induce considerably lift increase as they move along the surface, or trigger a catastrophic flow breakdown when taking off from the airfoil's surface.[3,4] In order to understand the mutual influence between these vortices and their interactions with the lifting surface, it is necessary to study not only their development in time but also their spatial correlation at each instant. In other words, quantitative information about the entire flow field is essential. This immediately excludes the use of traditional single-point measurement techniques, such as hot-wire anemometry or LDA. In view of this, a new experimental technique, Particle Image Displacement Velocimetry, herein abbreviated as PIDV, has been developed in our laboratory, which is capable of providing with great detail and accuracy about the instantaneous two-dimensional velocity and associated vorticity fields.[5]

The second part of this research involves a computational simulation of the Navier-Stokes equations using a discrete vortex, random walk scheme.[6] In general, the global flow features predicted by the computational scheme compare extremely well with the experiment.

2. Particle Image Displacement Velocimetry

PIDV technique can be regarded as a modified flow visualization method that is capable of providing quantitative data of the entire flow field. The operation of this technique involves the illumination of the flow field of interest, seeded with small tracer particles, with a thin laser light sheet as shown in figure 1. The light scattered by the seeding particles, which follow the local fluid motion, provided they are small enough, generates a moving particle-image pattern. This pattern is recorded using a multiple exposure photographic technique. The distance between the corresponding particle images being proportional to the local flow velocity. An optical Fourier transform is used to convert this spatial information into local velocity data. This process uses a focused laser beam to interrogate a small area of the multiple exposed photographic film. The diffraction pattern produced by the coherent illumination of the multiple images in the photographic transparency generates Young's fringes, in the Fourier plane of a lens, provided that the particle image-pairs inside the interrogating volume correlate, see figure 2. These fringes have an orientation that is perpendicular to the direction of the local displacement and a spacing inversely proportional to the displacement. A fully-automated process has been devised to acquire and analyze the fringe images at the Fluid Mechanics Research Laboratory of the Florida State University. The system consists of the following hardware components: a DEC MicroVax workstation II computer, Gould IP-8500 digital image processor, a frame digitizer, and a pipeline processor. For automatically scanning of the film transparency, a two-dimensional Klinger traversing mechanism with controller is used, see figure 3.

One important limitation of this method is that it is not possible to discriminate against the directional ambiguity introduced by the possible reversing motion in the flow field. To resolve this problem, a "velocity bias technique" has been proposed.[7,8] A uniform reference motion is added to the flow, thus superposing a velocity shift to the real flow field. A properly chosen shift can insure that all image displacements occur in the same direction, thereby eliminating the ambiguity. The true flow field can be recovered later by removing this artificial shift from the raw velocity data. The shift effect can be achieved by several methods; it can be done actively by using a rotating mirror, or passively by the use of a Calcite crystal.[9] In this work, a rotating mirror, General Scanning model # 6325D, with a scanner control, model # CX-660, is used to provide the image shift.

A dual pulsed laser system, consisting of two Spectral-Physics DCR-11 Nd-Yag pulsed laser systems, is used to provide the double pulses. As shown in figure 4, the light beams emitted from the two lasers are made collinear using a system of prisms and polarizing cube beam combiners. The second laser is triggered by the first laser via a Systron Donner 100C pulse generator. Separation between the pulses can be varied from a fraction of one μsec. to a few seconds by adjusting the pulse generator. A cylindrical lens is used to project the combined beam into a laser sheet to illuminate the mid-span section of the airfoil. Metallic coated particles (TSI model 10087), with an average diameter of 4 μm, were used as the flow tracers. A 35 mm camera (Nikon F-3) was used to record the flow field.

The pulsed lasers were triggered continuously at a frequency about 10 hertz in order to utilize their full power. That means the scanning motion of the mirror and the camera

shutter release should also be phase-locked to that frequency. Due to this restraint, the time interval between pictures had to be chosen to be a multiple of the laser pulsing period, and it was set at 0.3 second for this experiment. Synchronization between components was accomplished by using the Tektronix modular electronics system as shown in figure 5. On the other hand, this system also provided the phase-reference between the motion of the airfoil and the PIDV photographic timing sequence , see figure 6.

3. Experimental Facility

The experiments were performed in a towing water tank facility, which is 1.8 meter long and 43 by 55 cm in cross-sectional area. The towing carriage was driven by a DC servo motor with a towing speed varying from 0.3 to 30 cm/sec. A NACA 0012 airfoil with a chord length of 6 cm and an aspect ratio of 6.67, is used. This corresponds to a Reynolds number between 200 and 20000, based upon the towing speed and the airfoil's chord. The towing speed was controlled by a motor speed control system, Electro-Craft model # E-652, via digital-to-analog converter. Acceleration and deceleration ramps were included for smooth traverse. The airfoil's pitching motion was provided by a Klinger stepping motor with a programmable controller, Klinger model CC-1.2, which was pre-programmed and activated by the host computer. The airfoil's angle changed linearly from 0 to 30° after the airfoil had been towed for more than one chord length and presumably had established a steady-state travel. All motions were monitored by a DEC Vaxstation II computer, see figure 6.

4. Numerical Simulation Scheme

Random-walk vortex simulations of the full Navier-Stokes equations were performed for a comparison with the PIDV data. In the computations, the flow field was represented by discrete vortex blobs. The diffusion processes were simulated by adding a random component of magnitude $\sqrt{2\nu\Delta t}$ to the vortex motion.

In the method, no accuracy is lost in describing the strong convection process typical of unsteady separated flows. Additionally, the computational domain is truly infinite; there are no artificial boundary conditions. But most importantly, since computational elements are only used in the limited regions containing appreciable vorticity, the resolution, (the smallest scales the computation can distinguish), is very high.

The fast solution-adaptive Laurent series technique[10] was used to allow a large number of vortex blobs to be included without using a mesh-based fast solver to find the velocity.

The normal wall boundary condition was satisfied by mirror vortices, after a mapping of the airfoil onto a circle. The mapping used was a generalized Von Mises transform which exactly reproduces the slightly blunted trailing edge of the NACA 0012.

The no-slip boundary condition was satisfied by the addition of vortices at the wall dur-

ing each time-step. First all vortices within a distance of $1.27\sqrt{2\nu\Delta t}$ were removed. Then a ring of new vortices was added at a distance $0.675\sqrt{2\nu\Delta t}$ to correct the wall slip to zero. (The distance for adding vortices equals the diffusion distance of the vorticity generated by the wall during the time-step for the true Navier-Stokes equations; the removal distance was chosen based on a statistical study requiring that the scheme handles locally uniform vorticity distributions accurately, not unlike discretization techniques in finite difference procedures). The vortex diameter was rather arbitrarily chosen to be $0.675\sqrt{2\nu\Delta t}$; testing showed that results depended little on the actual value used.

In order to allow pitching motion, the equations of vortex motion were developed in an inertial reference frame and subsequently converted to an airfoil based system. This is required since Kelvin's theorem cannot be used in a rotating coordinate system. The force on the airfoil is found from differentiating integrals of the vorticity distribution, rather than directly from the wall shear and pressure.

The CYBER 205 results were post-processed on a MicroVax II computer, using a fast Fourier transform to find the streamlines. The vorticity was represented in bit-mapped graphics as half-tones. The dimensionless pitch rate and the Reynolds number are chosen to be exactly the same as those in the experiments for readily comparison.

5. Results and Discussion

5.1 PIDV Data

Reynolds number calculated with the chord length and the free-stream velocity is 5000 for all the results presented. The airfoil is pitching up from an angle of attack of 0 to 30 degrees with a dimensionless pitch rate $\dot{\alpha}$, normalized by the airfoil's chord and free-stream velocity, of 0.131. The unsteady flow development over the airfoil after the pitch-up is presented sequentially from figures 7-(a) to 7-(d). The velocity field data in these figures is acquired in a Cartesian mesh by digitally processing the fringes, produced by point-by-point scanning of the film transparency. The length of each vector is proportional to the local velocity at that point. Also shown is the vorticity level superimposed on the velocity field by using the color code.† The magnitude of the vorticity is given by the color bar at the left lower corner of the figures. The red and purple colors represent the peak levels of the positive (clockwise) and negative (counterclockwise) vorticity.

In figure 7-(a), the airfoil has travelled about 1.27 chord length after the initial pitch up and reaches an angle of attack of 7°, which is below the 12° static stall angle for the NACA 0012 airfoil within this Reynolds number range. There is no noticeable flow development on both the upper and lower surfaces of the airfoil. On the upper surface, boundary layer is slightly thickening with no distinguishable separation. Near the trailing edge, strong negative vorticity has been shed from the lower surface as a result of the airfoil's pitching up motion.

As the airfoil continues to move to about 2.98 chords downstream and at an angle of 20°, which is well beyond the static stall angle, separation start to develop on the upper surface, as shown in figure 7-(b). Near the leading edge, flow separates and reattaches downstream forming a recirculating eddy, which occupies approximately a quarter of the chord. Near the mid-chord of the airfoil, the reattached boundary layer separates again, forming another recirculation eddy that almost covers the entire downstream section. Strong flow reversal can be seen from the trailing edge all the way to about the mid-chord region. On the other side of the airfoil, flow appears to behave smoothly. There is no significant flow breakdown at this stage although the airfoil has already gone beyond the static stall condition.

Not until further downstream, after the airfoil has moved 5.13 chords and reaches its maximum angle of 30°, massive flow separation starts to develop, see figure 7-(c). The leading edge separation bubble grows into a large scale vortex and moves downstream. It induces very strong reverse flows along the airfoil's surface, which can be of the same order of magnitude compared to the free-stream. Interestingly, the reversing flows carry very low level of vorticity as shown by the color code for the vorticity level.

The vortical structure simply rides on this upstream-moving stream. An important consequence is the slowdown of the convection process of the vortex. Following the primary vortex is a series of smaller vortices, which form as a result of the vorticity accumulation of the shear layer that is separating from the leading edge. Under the shear layer vortices and very close to the surface of the airfoil, there are two secondary vortices which have

† Vorticity contour plot will be used for the final mat

the opposite sign of rotation as the vortices right above them. Downstream of the primary vortex, local flows have been propelled to attach onto the airfoil's surface immediately before the trailing edge. This suggests the existence of a stagnation point immediate before the trailing edge. Away from the airfoil, outer flow stream still shows an overall convex curvature, suggesting that the global circulation is preserved and the lift of the airfoil can be maintained or increased even after massive flow separation.

In figure 7-(d), the primary vortex eventually takes off from the trailing edge, at a location of 7.27 chord length after the initial pitch-up, triggering the entire flow into complete breakdown. The primary vortex can be barely observed at the right upper corner in figure 7-(d) as it is gradually leaving the scene. A strong counter-rotating vortex is shed from the lower surface and starts to roll up near the trailing edge and penetrates into the upper surface. Flows separate from the leading edge forming a shear layer without reattaching downstream. An open wake is formed, accompanied by the plunge of the circulation around the airfoil, which characterizes the final stage of the stall of the airfoil. A concave overal curvature suggests a loss of the airfoil's lift.

5.2 Computational Results

Typical two-dimensional computational results from random-walk vortex simulations of the full Navier-Stokes equations are shown in figures 8-(a) to (i). The Reynlods number, the dimensionless pitch rate and the maximum angle of attack are the same as those in the experiment. The only difference is the way the airfoil is pitched. Since a linear pitch-up profile, as adopted in the experiment, will lead to an infinite loading on the airfoil in the computational scheme, consequently, a smooth profile with continuous curvature, which is fitted by a fifth-order polynomial, is chosen instead. Therefore, comparison between the experiment and computational simulation can be considered only qualitatively rather than quantitatively. The instantaneous streamline pattern, along with vorticity field that is represented in bit-mapped graphics as half tones, are shown. In general, the simulated patterns agree well with the experimental data.

In figures 8-(c) and 8-(d), corresponding to $\alpha = 21.7°$ and $26.9°$, respectively, the existence of two vortical eddies agrees with the experiment, see figure 7-(b). The leading edge eddy ends as the separating leading edge shear layer reattaches downstream and re-separates again at mid-chord to form a larger size bubble occupying the downstream half of the airfoil. As this vortex approaches the trailing edge, a counter-rotating vortex is shed from the lower surface. This exactly matches the experimental observation as shown in figure 7-(b).

The leading edge vortex grows and moves downstream in exactly the same manner as revealed from the experiment, compare figures 8-(e) and (f) to figure 7-(c). The size of the primary vortex also compares favorably to the experiment. Other distinct features, such as the formation of the shear layer vortices following the primary vortex and the development of a counter-rotating vortex near the surface, have also been faithfully simulated. As demonstrated in figures 8-(e) and (f), Vortex dynamics appears to play an important role as the primary vortex interacts strongly with the shear layer vortex that immediately follows it as they begine to evolve downstream. By associating the discrete vortex simulation with

the whole-field PIDV measurement, for the first time, this very complex process can be carefully analyzed.

The breakdown process appears to begin with the shedding of a counter-rotating vortex near the trailing edge as the primary vortex is moving away from the airfoil, see figure 8-(g). The situation aggravates as the flow completely separates from the airfoil as shown in figures 8-(h) and 8-(i). The emergence of a concave curvature can be seen as a sign that indicates a total loss of circulation and, consequently, the lift.

Summary

PIDV is capable of providing the velocity and associated vorticity fields with good spatial resolution and accuracy of a very complex unsteady flow field, that is the unsteady flow past an impulsively pitching-up airfoil. Noticeable flow separation develops when $\alpha > 20°$, which is well beyond the static stall angle, with one separation bubble near the leading edge and another eddy presides over the trailing edge region. The development of the leading edge vortex dominates the later flow behaviors. This vortex grows, to a size that is comparable to the airfoil's chord, and moves downstream. Outer flow maintains its convex curvature while the vortex is accumulating its strength; the lift is still increasing. A counter-rotating vortex is released from the trailing edge as soon as the primary vortex detaches from the surface, triggering the airfoil into stall. Strong flow separation prevails and flow separates from the leading edge without downstream reattachment. Surrounding flow has a concave curvature and the airfoil's circulation, along with its lift, drop.

A discrete vortex, random walk computation was undertaken to augment the experimental studies. In general, the simulation results agree extremely well with the experiment.

Acknowledgments

This program is supported by the Air Force Office of Scientific Research.

Final Remarks

As you may have already known, data analysis for the PIDV is quite different from the traditional experimental technique: data collection is undertaken after the completion of the experiment. For now, we have already finished our experiment but our analysis system has been occupied by other project, therefore, we can only provide a small portion of the data we collected. The complete data, which should include data sets with much finer time sequence for a Reynolds number of 1400 and 5000.

References

1. W.J. McCroskey, "Unsteady Airfoils", Ann. Rev. Fluid Mech. Vol. 11, 1982, pp 285-311.

2. W.C. Reynolds and L.W. Carr, "Review of Unsteady, Driven, Separated Flows" AIAA paper no. 85-0527, 1987.

3. C. Shih, M. Lee, and C.M. Ho, "Unsteady Separation over Two- and Three-Dimensional Airfoils", Proceeding of Workshop on Unsteady Separated Flow, July 1987, Colorado Springs, Colorado, pp 38-41.

4. K.W. McAlister and L.W. Carr, "Water-Tunnel Experiments on an Oscillating Airfoil at Re = 21,000", NASA TM 78446, March 1978.

5. A. Krothapalli and L. Lourenco, "Unsteady Separated Flows: A Novel Experimental Approach", AIAA paper 87-0459, 1987.

6. L.L. Van Dommelen, "Lagrangian Techniques for Unsteady Flow Separation", Forum on Unsteady Flow Separation, 1987 ASME Applied Mechanics, Bioengineering and Fluids Engineering Conference, June 14-17, 1987, Cincinatti, OH., pp. 81-84.

7. L. Lourenco, "Application of Laser Speckle and Particle Image Velocimetry in Flows with Velocity Reversal", Bull. Amer. Phys. Soc., Vol. 31, no. 10, 1986, pp. 1723.

8. R.J. Adrian, "Image Shifting to Determine the Polarity of Velocity Vectors Measured by Pulsed Laser Anemometry", Bull. Amer. Phys. Soc., Vol. 31, no. 10, 1986, pp. 1722.

9. L. Lourenco, "A Passive Velocity Bias Technique for PIDV", Bull. Amer. Phys. Soc., Vol. 34, no. 10, 1989, pp. 2267.

10. L.L. Van Dommelen and E.A.Rundensteiner, "Fast Solution of the Two-Dimensional Poisson Equation with Point-Wise Forcing", to appear in the Journal of Computational Physics.

æ

p

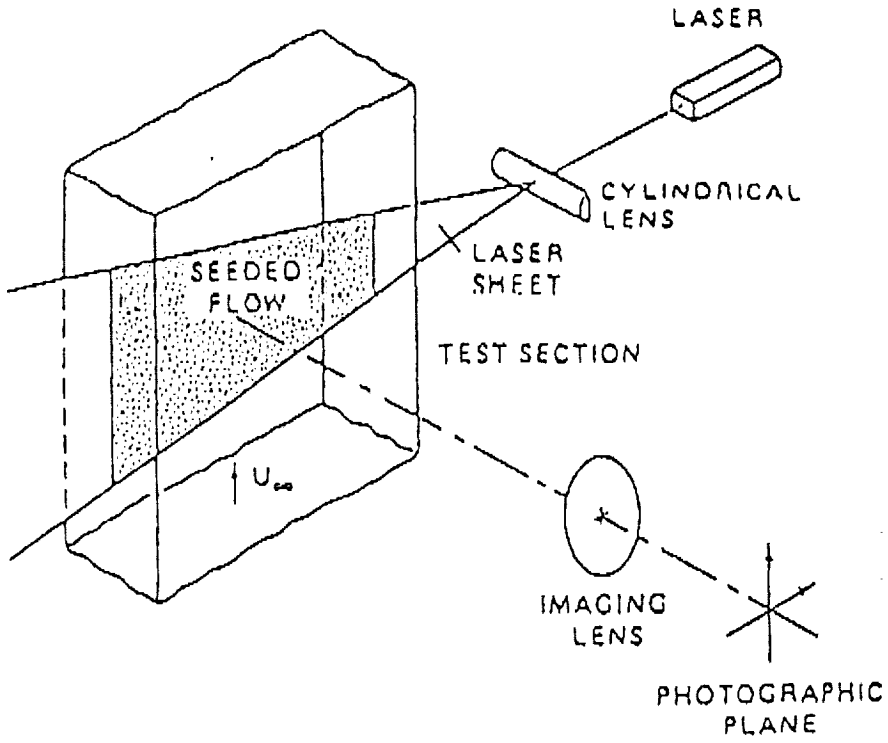

Figure 1. Schematic arrangement for the photographic recording.

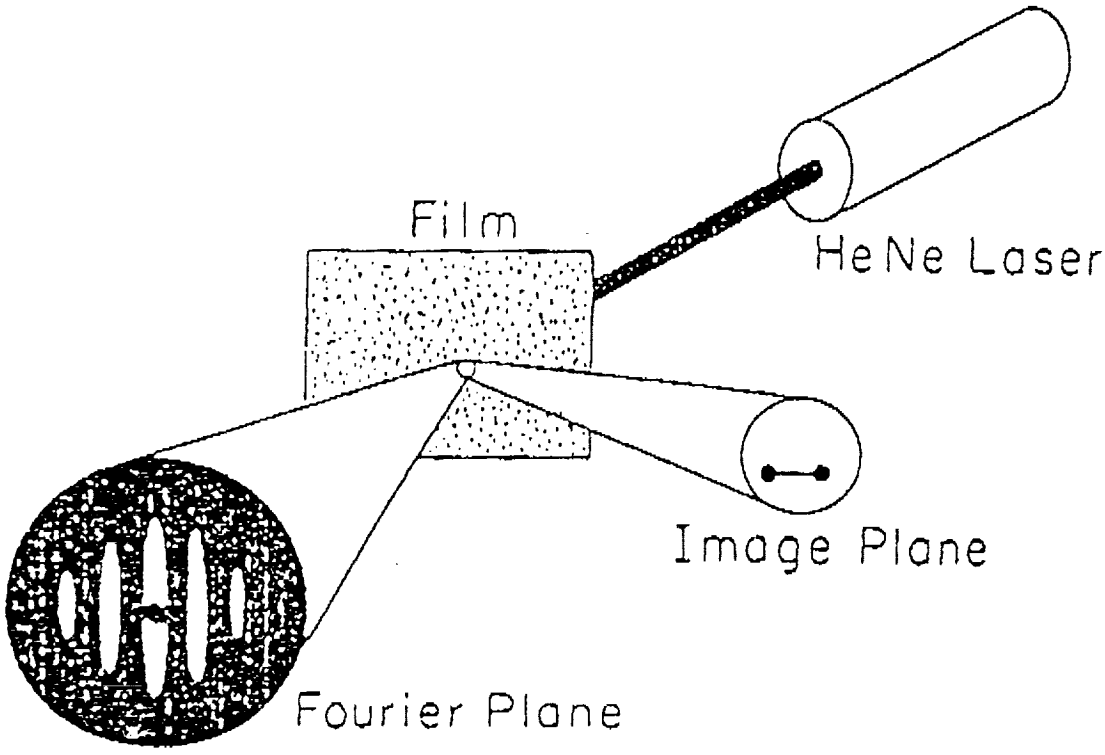

Figure 2. Schematic arrangement for obtaining Young's fringes.

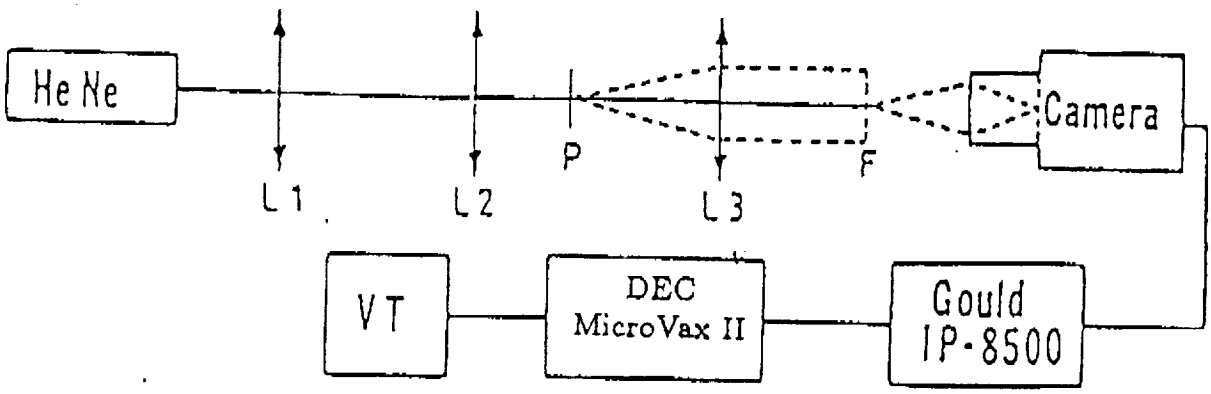

Figure 3. Schematic of the data analysis system

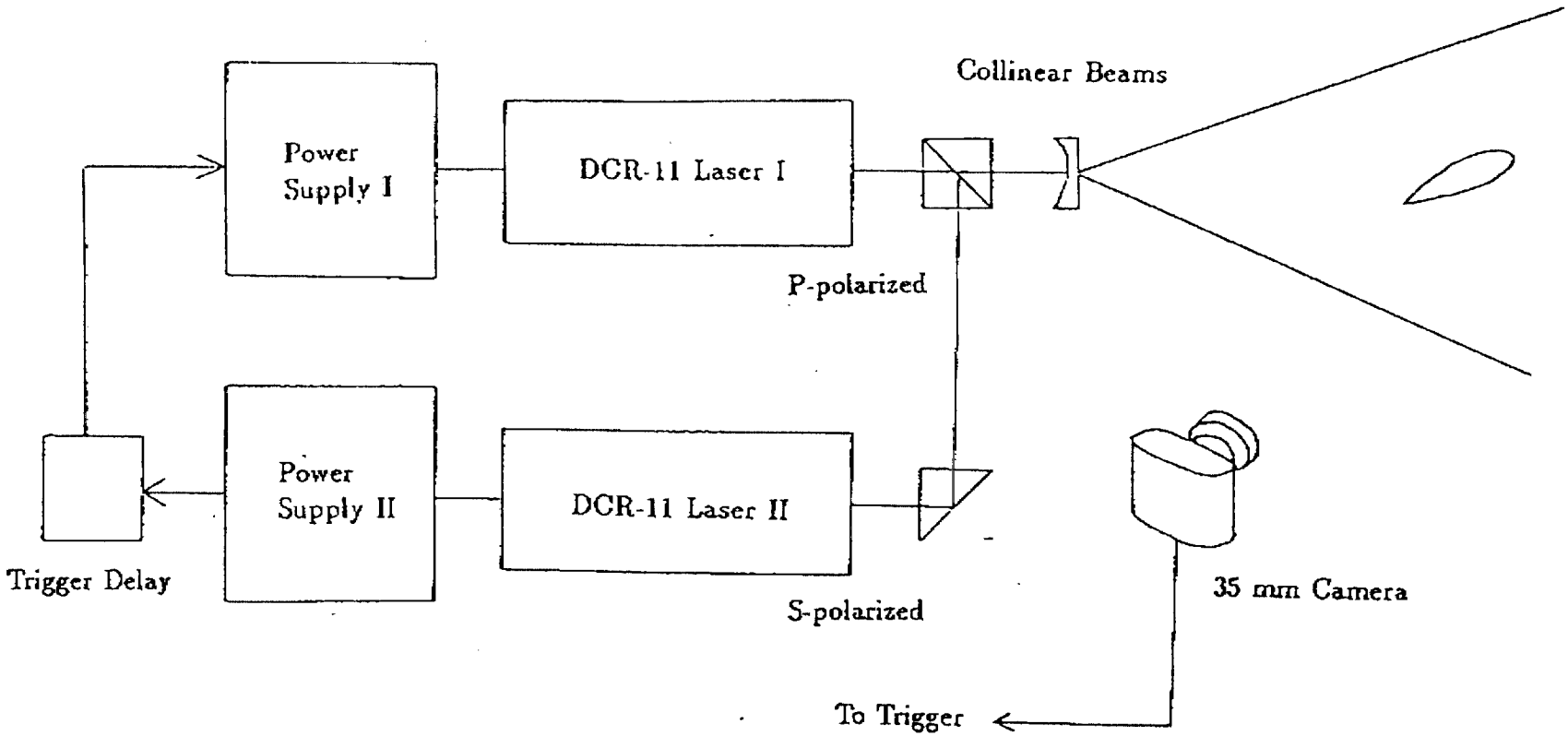

Figure 4. Schematic arrangement for the dual pulsed-laser system

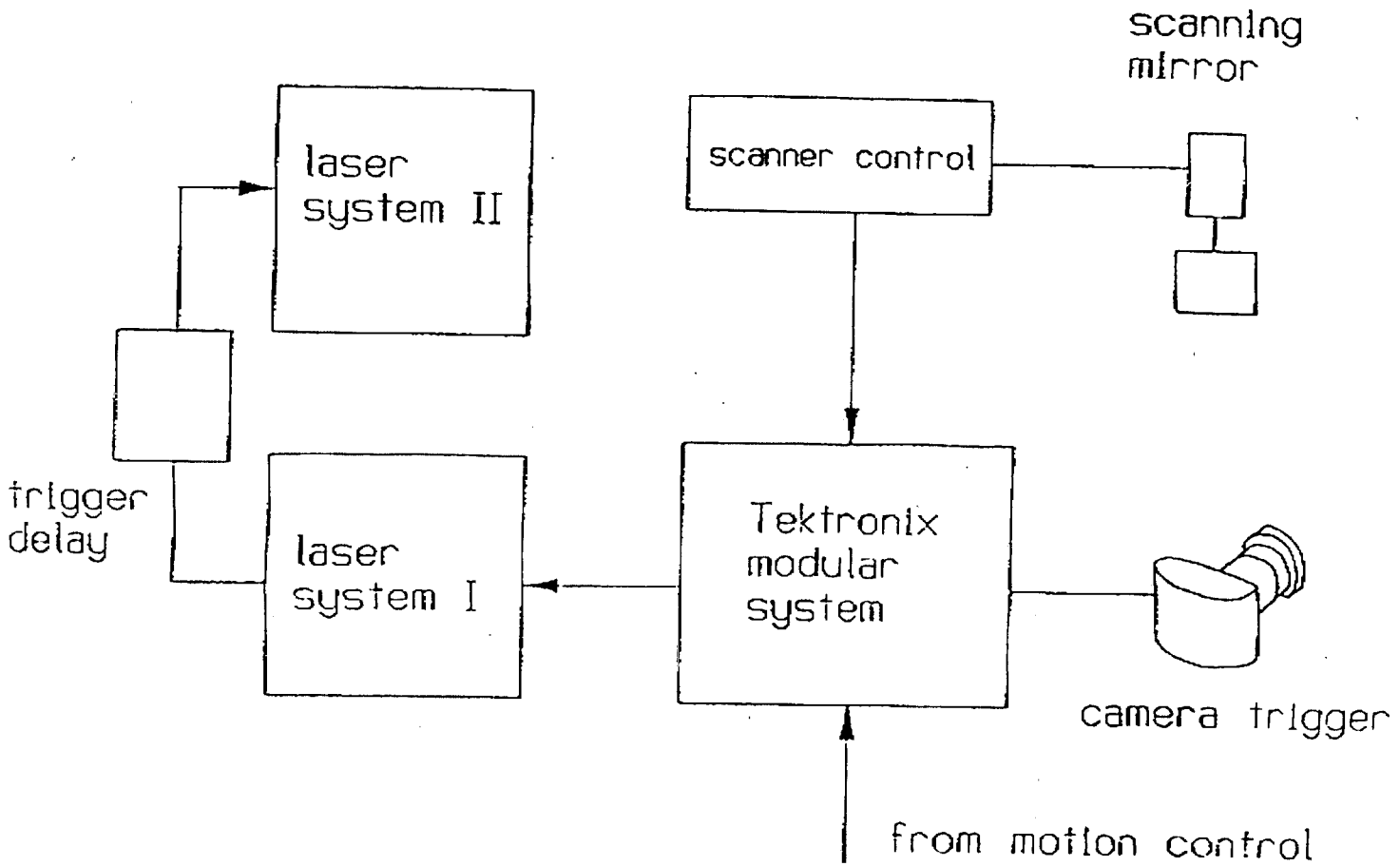

Figure 5. Synchronization arrangement for PIDV

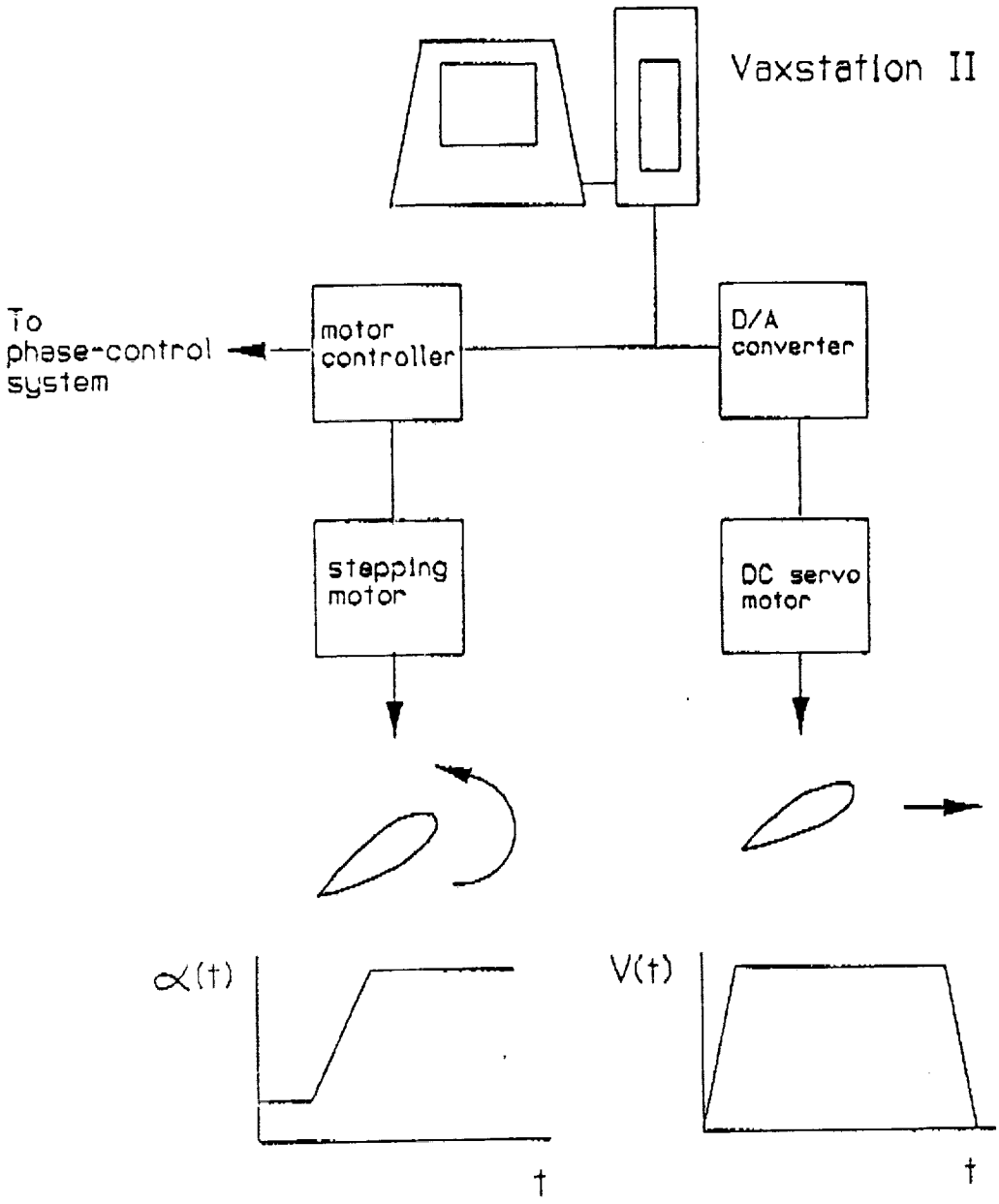

Figure 6. Schematic of the airfoil's motion control system

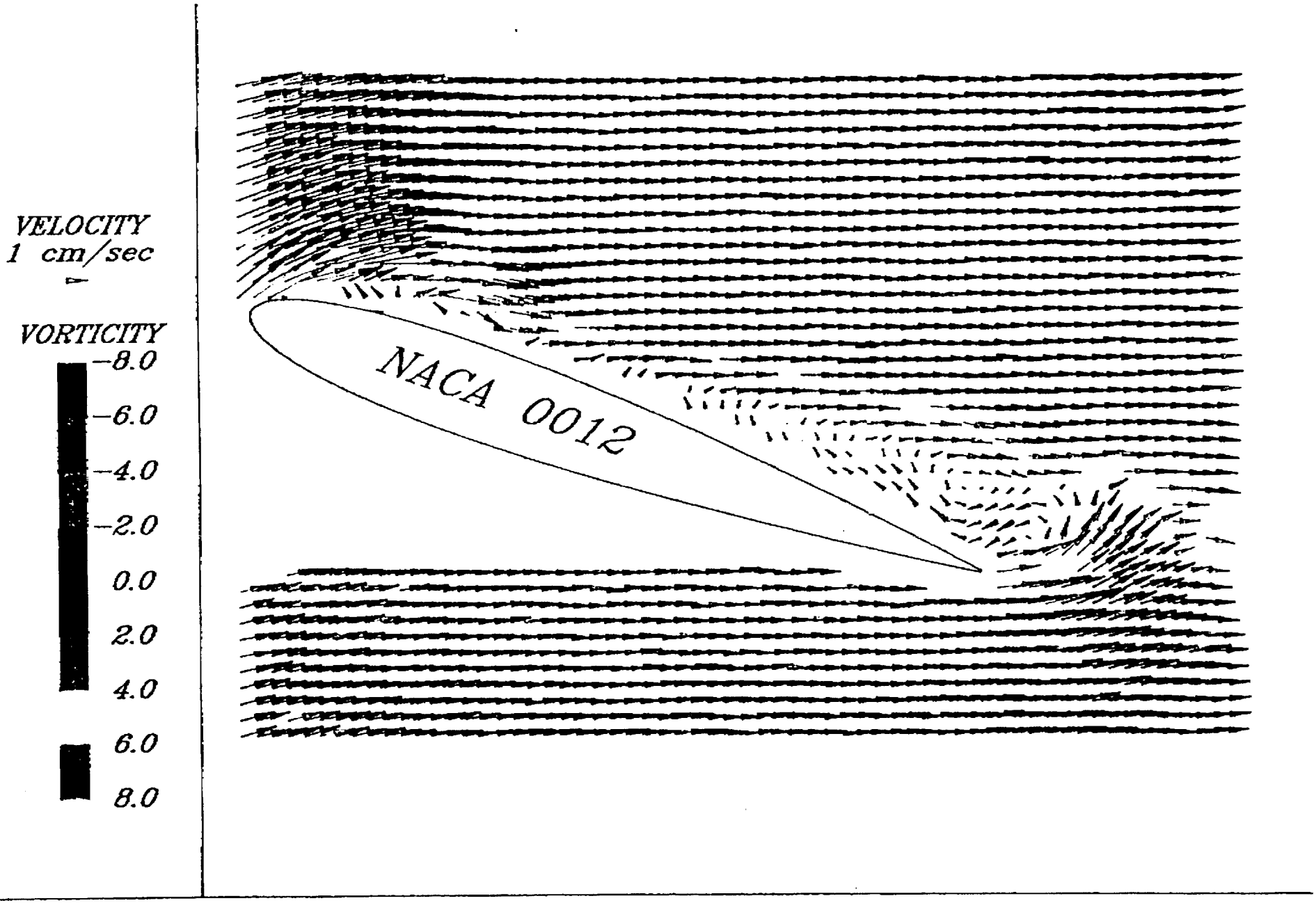

(b) $t^* = 2.98$, $\alpha = 22.4°$;

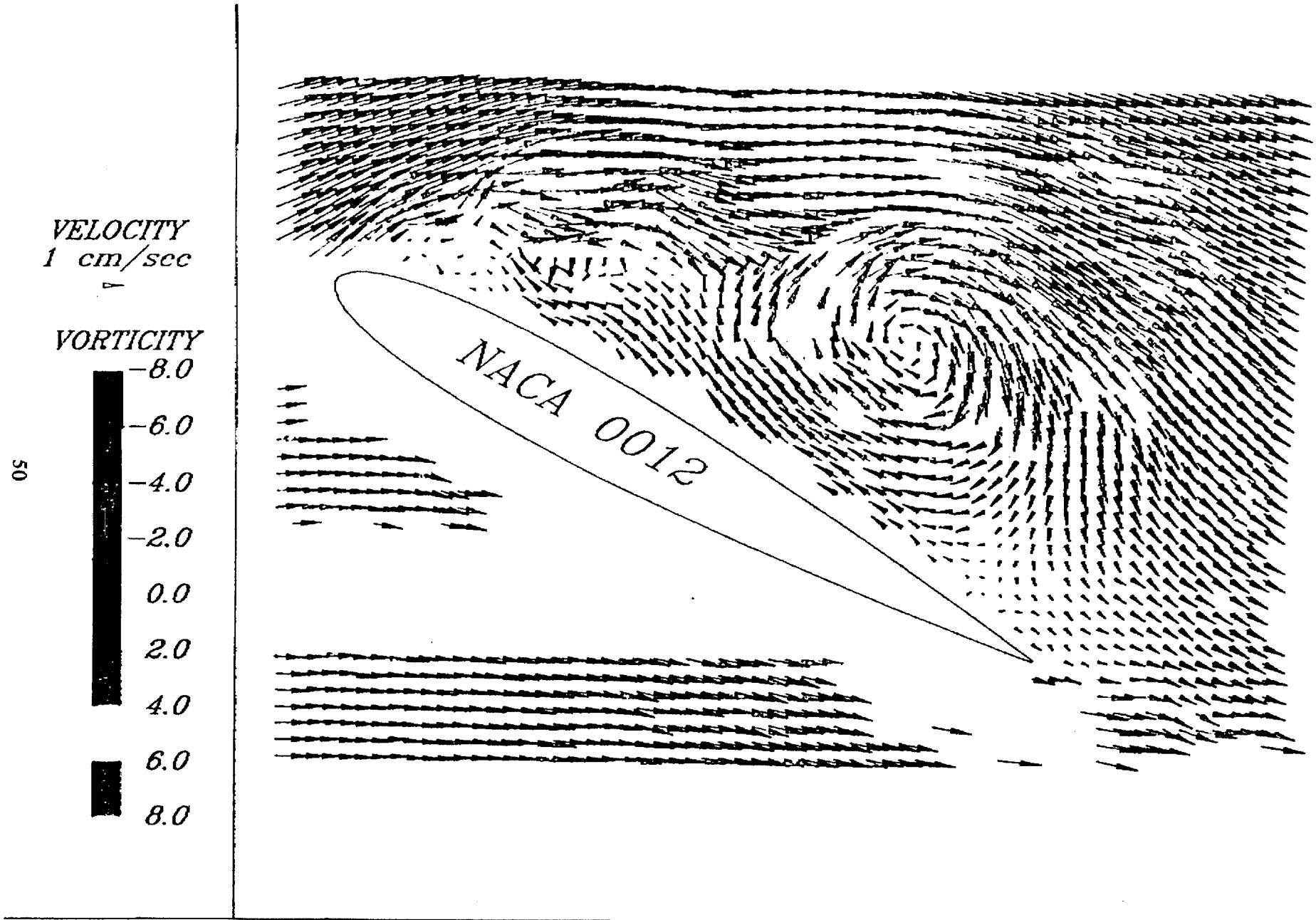

(c) $t^* = 5.13$, $\alpha = 30.0°$;

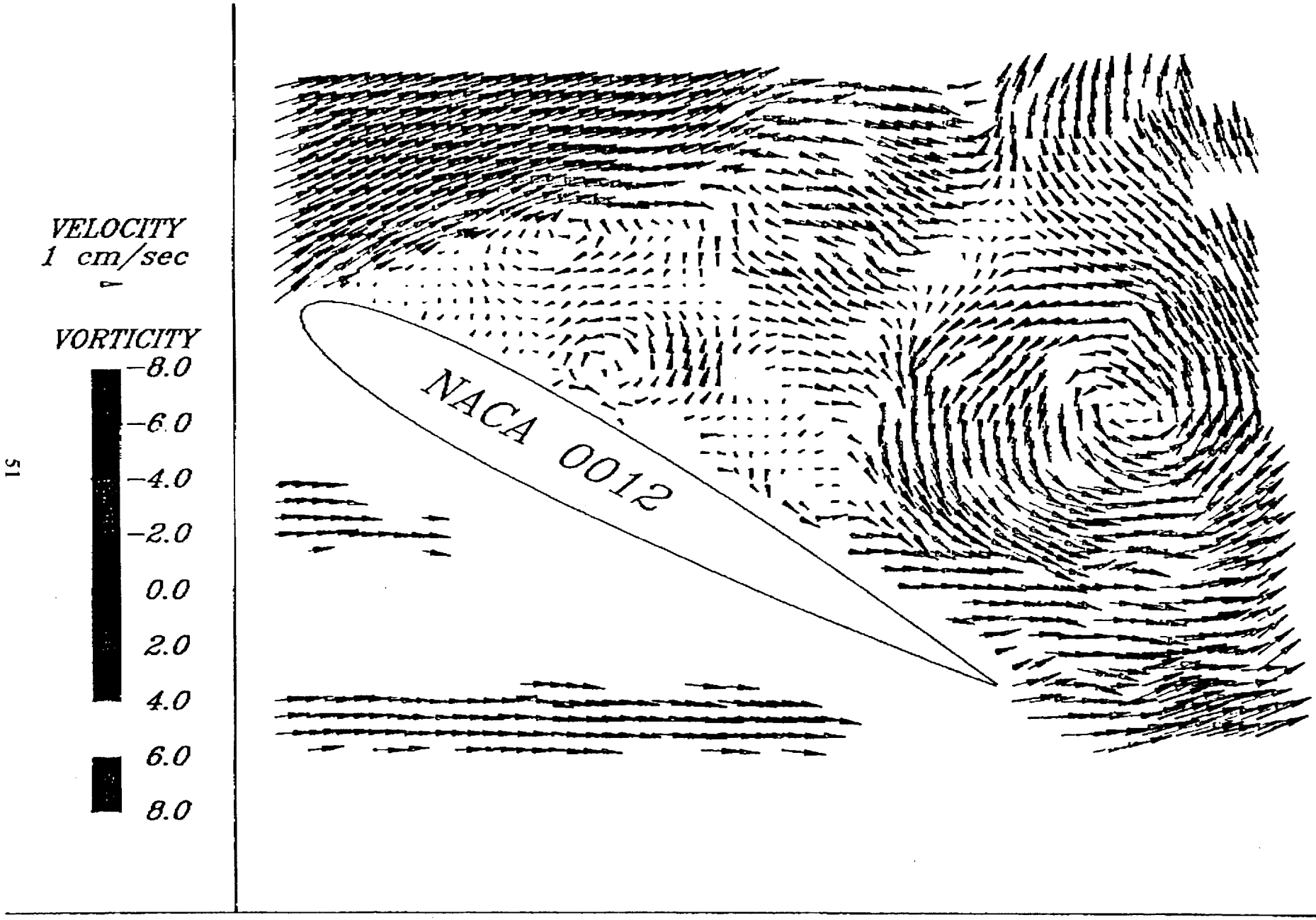

(d) $t^* = 7.27$, $\alpha = 30.0°$.

Figure 7 Time evolution of the instantaneous velocity and associated vorticity fields measured by the PIDV. Re = 5000. $\dot{\alpha} = 0.131$, $t^* = \frac{tU_\infty}{c}$

(a) $t^* = 1.5$, $\alpha = 8.3°$;

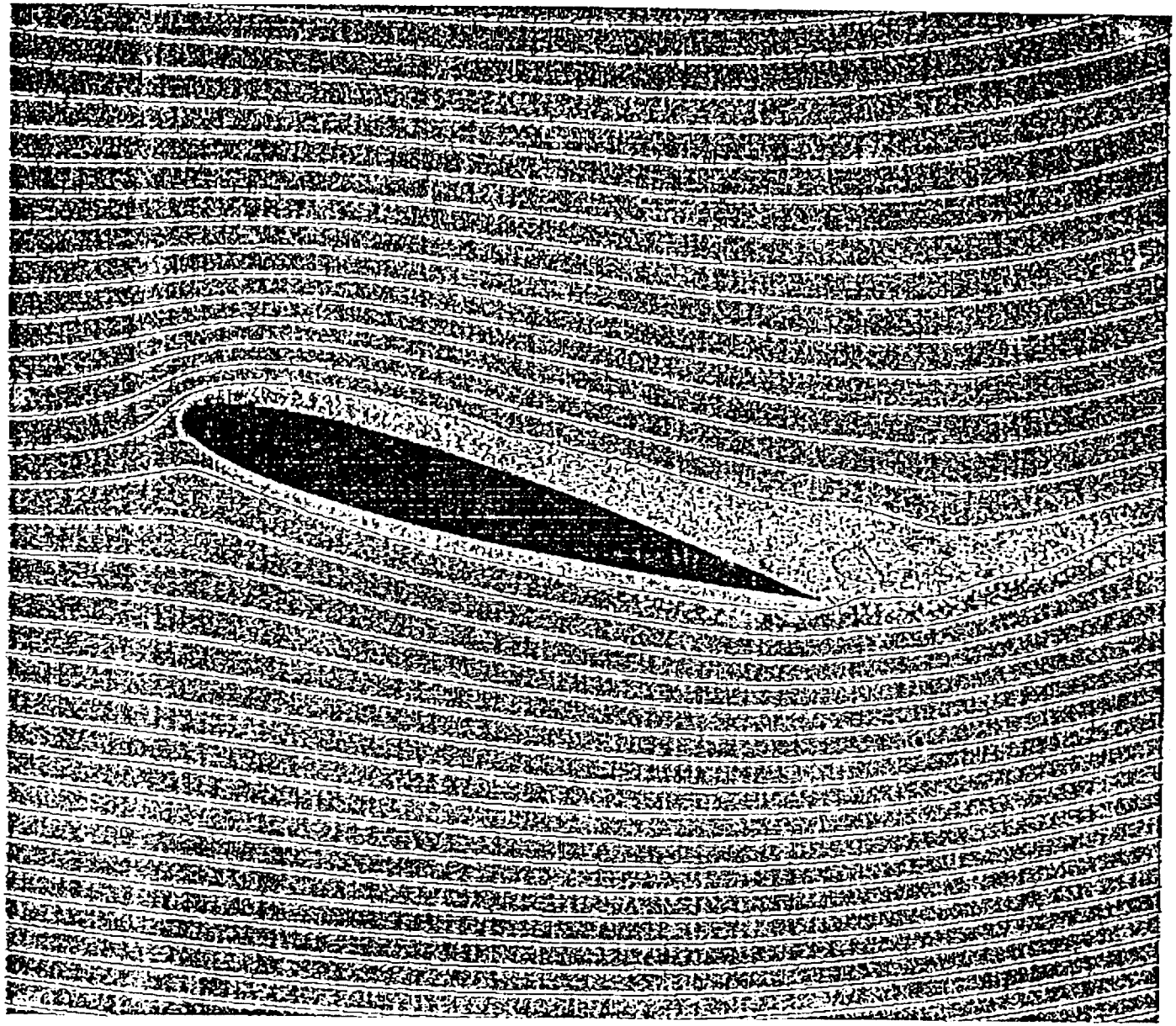

(b) $t^* = 2.0$, $\alpha = 15.0°$;

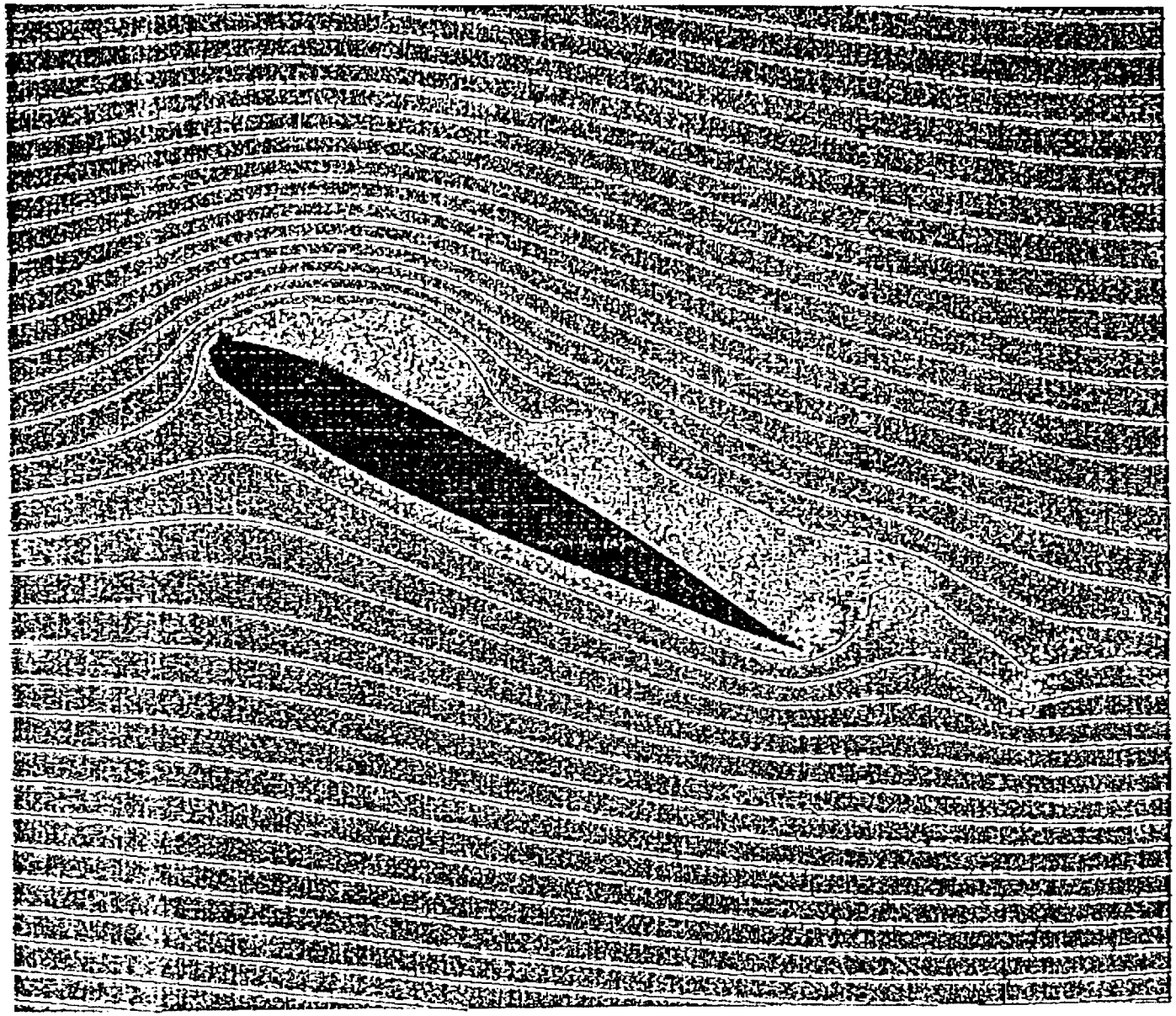

(d) $t^* = 3.0$, $\alpha = 26.9°$;

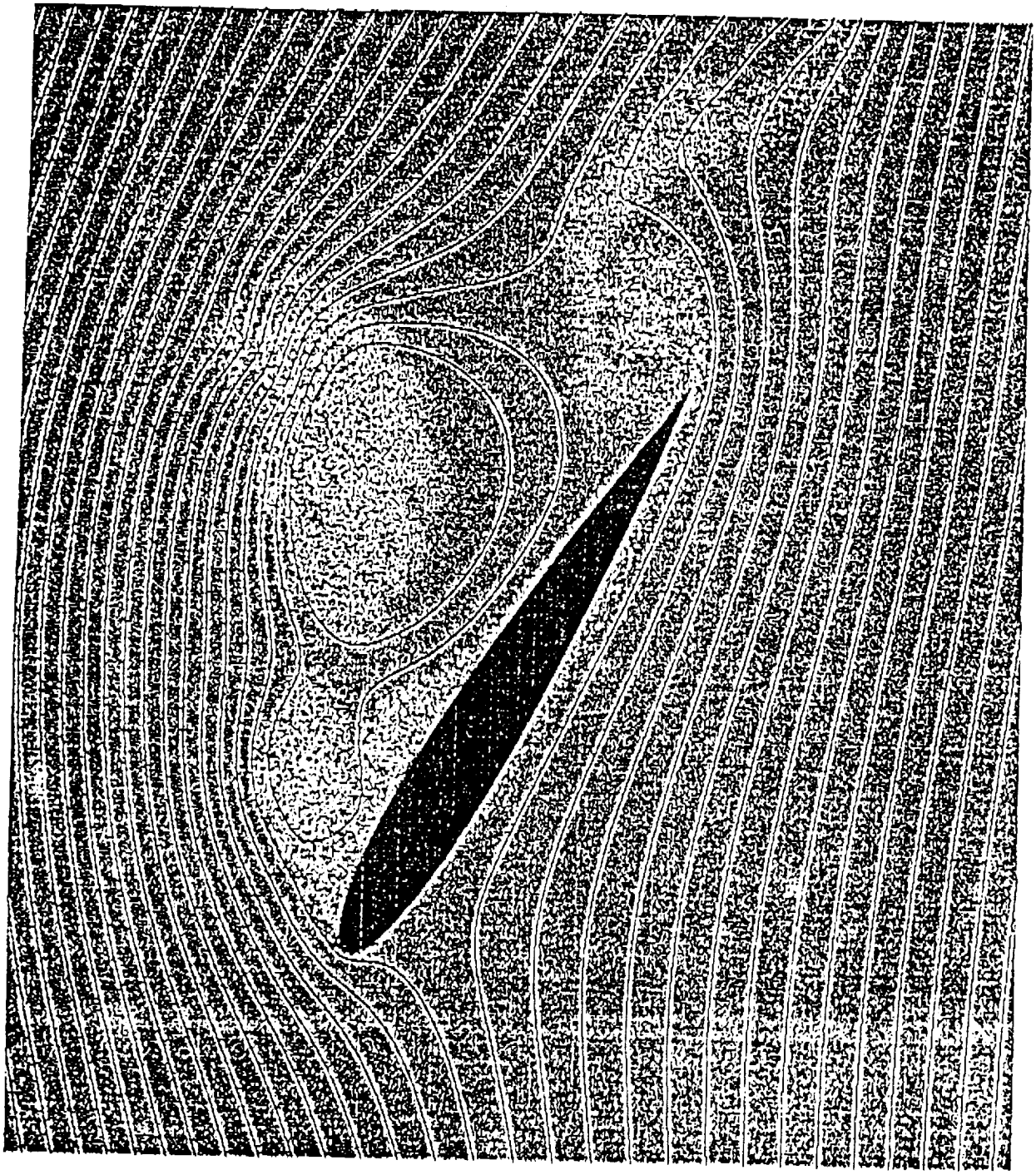

(c) $t^* = 4.5$, $\alpha = 30.0°$;

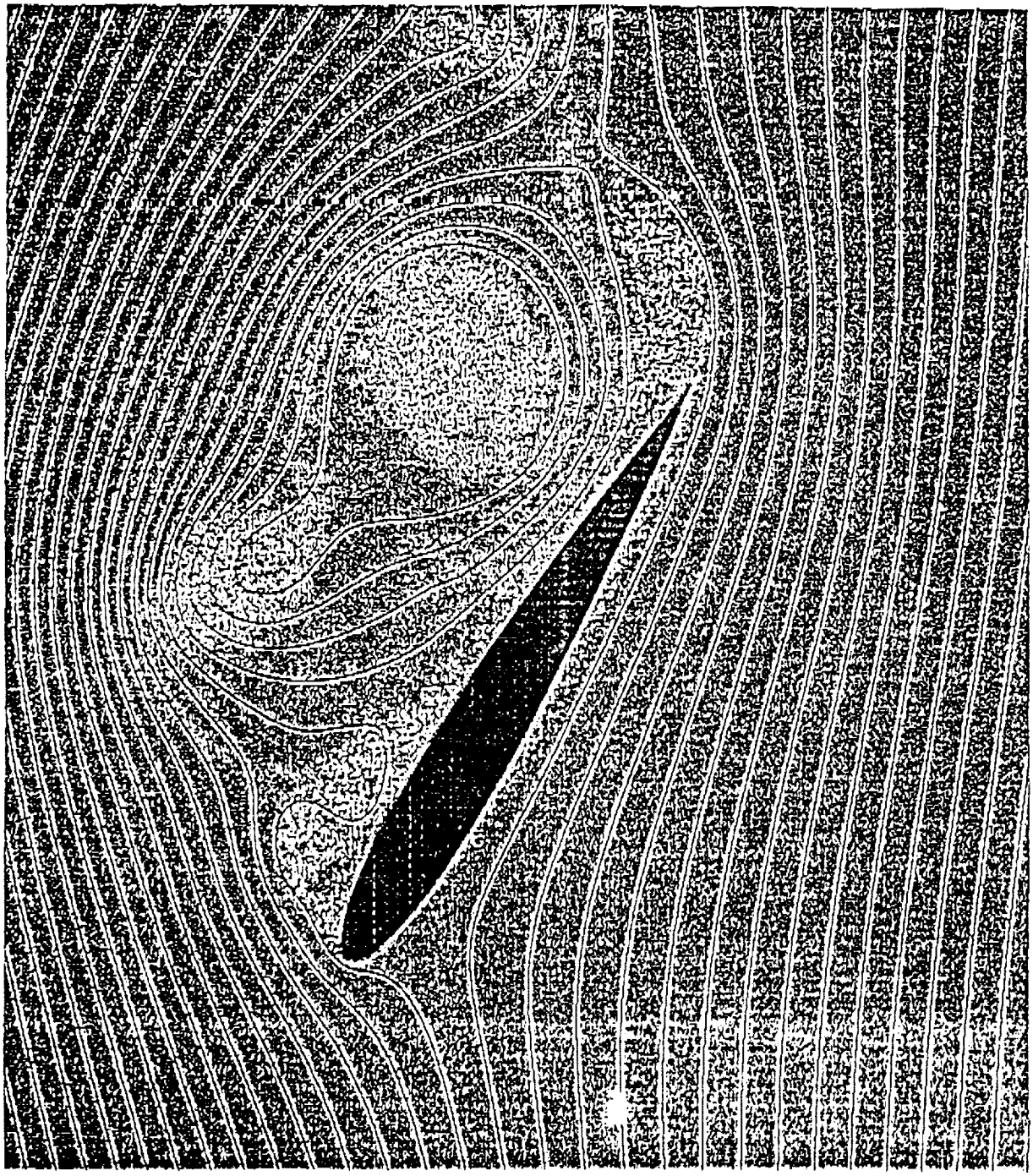

(f) $t^* = 5.0$, $\alpha = 30.0°$;

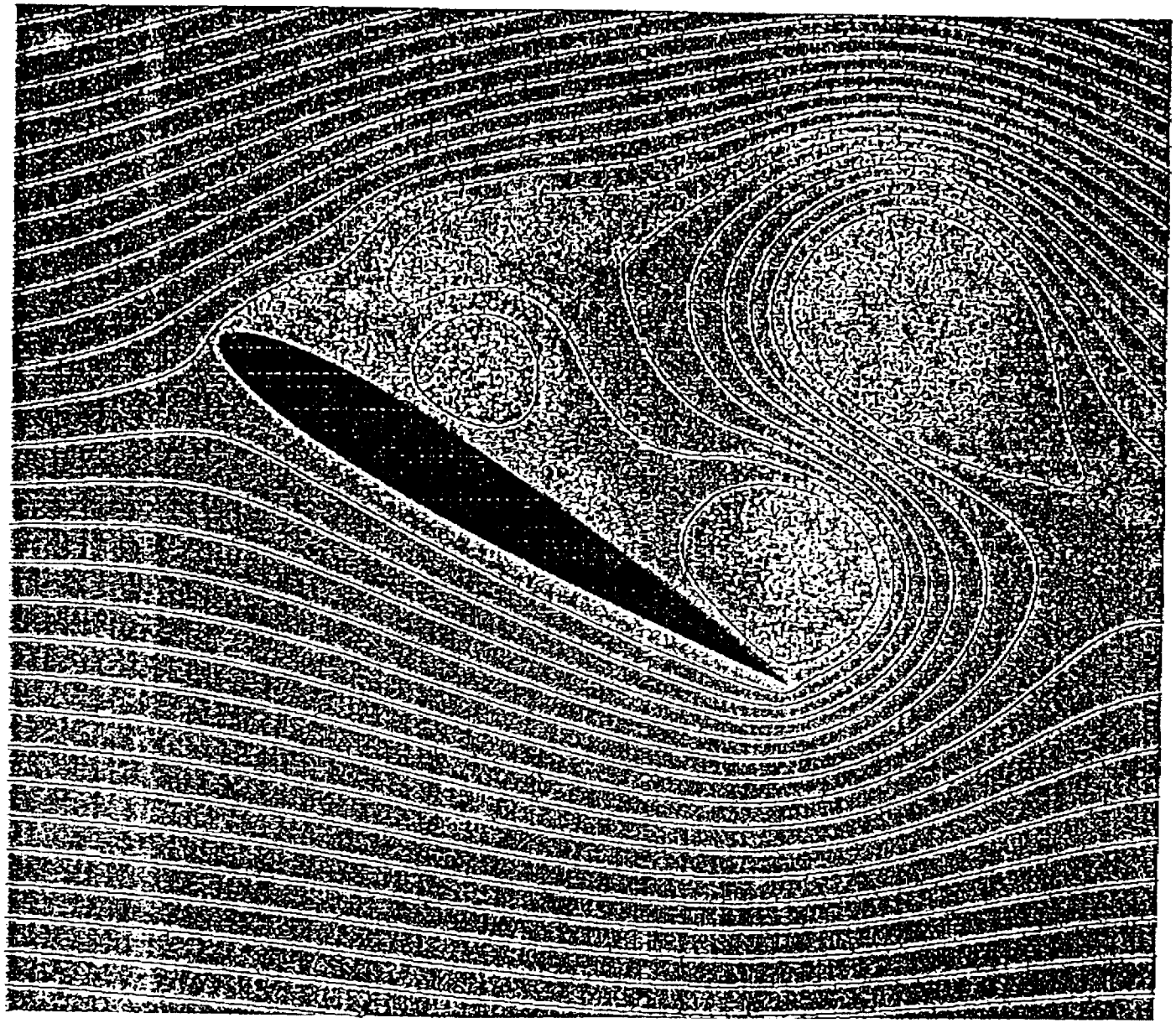

(g) $t^* = 6.0$, $\alpha = 30.0°$;

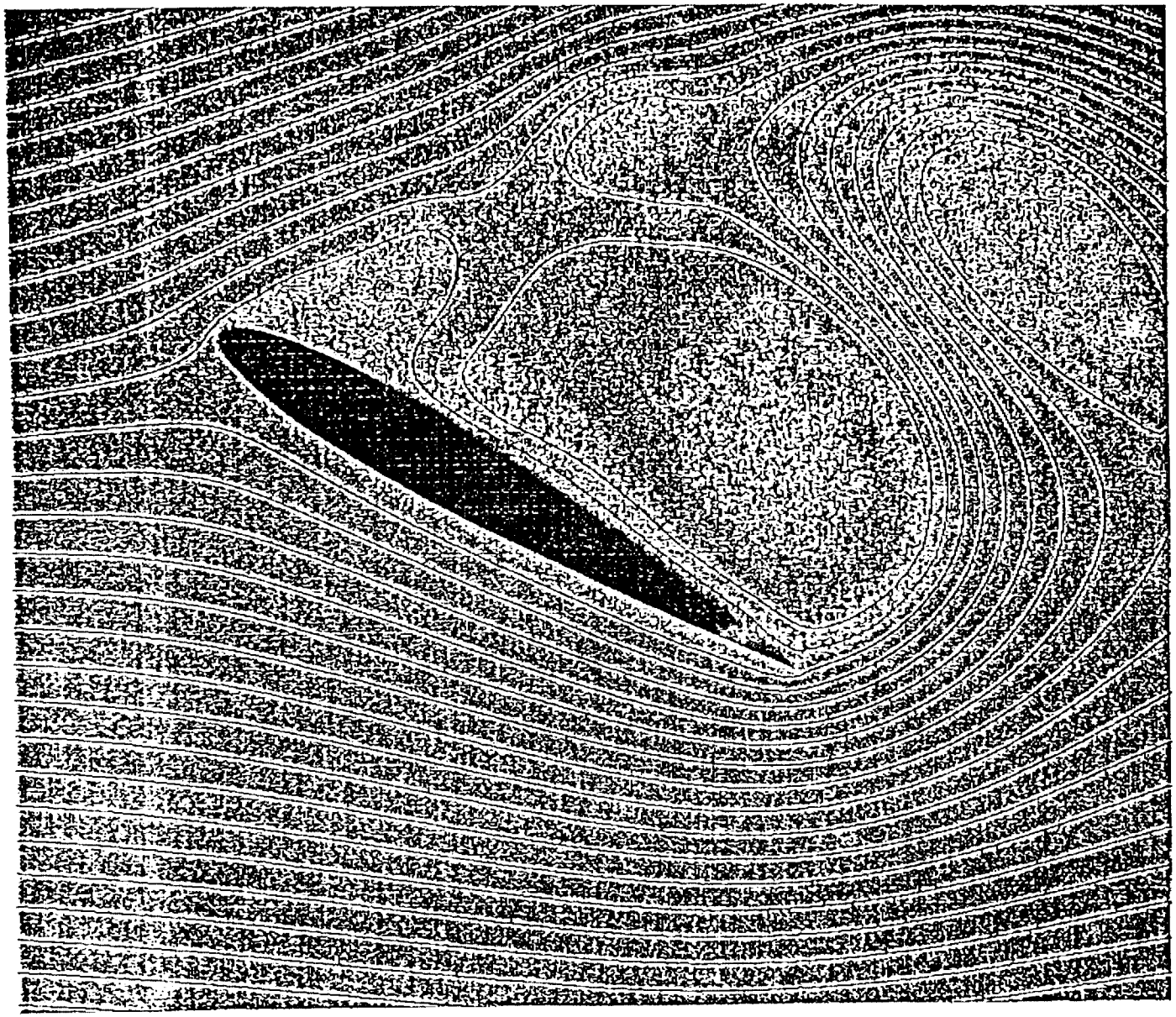

(h) $t^* = 6.5$, $\alpha = 30.0°$;

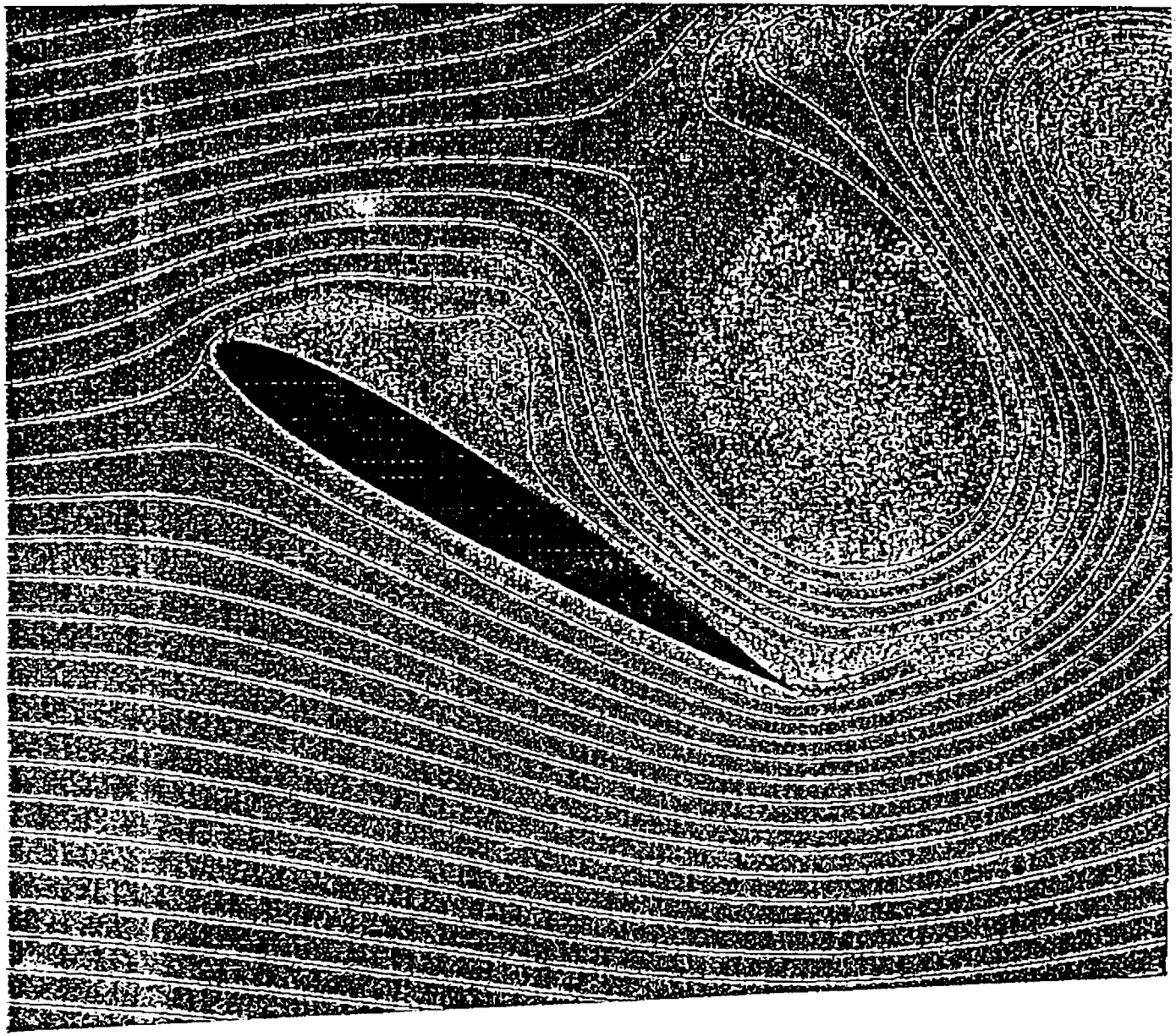

(i) $t^* = 7.0$, $\alpha = 30.0°$.

Figure 8. Computational results of the instantaneous streamline pattern and associated vorticity distribution. Re = 5000. $\dot{\alpha} = 0.131$.